Combined microwave analysis of vortex pinning and HAADF-STEM structural characterization of YBCO films with columnar defects

18 (2026) 100265

Contents lists available at ScienceDirect

Superconductivity

journal homepage: www.elsevier.com/locate/supcon

Research Article

Combined microwave analysis of vortex pinning and HAADF-STEM structural characterization of YBCO films with columnar defects

Gianluca Ghigo [a,b,*], Mario Scuderi [c,d], Michela Fracasso [a,b], Roberto Gerbaldo [a,b], Daniele Torsello [a,b], Laura Gozzelino [a,b]

[a] Department of Applied Science and Technology, Politecnico di Torino, Torino, 10129, Italy
[b] Istituto Nazionale di Fisica Nucleare, Sezione di Torino, Torino, 10125, Italy
[c] CNR-IMM, Catania, 95121, Italy
[d] Istituto Nazionale di Fisica Nucleare-LNS, Catania, 95123, Italy

ARTICLE INFO

Keywords:
Microwave superconductivity
Heavy ion irradiation
YBaCuO films
HAADF-STEM imaging
Vortex pinning
Columnar defects
Microwave coplanar resonators

ABSTRACT

We report on a systematic investigation of the effects of columnar defects induced by heavy ion irradiation in $YBa_2Cu_3O_{7-\delta}$ thin films. The study encompasses their structural characterization by transmission electron microscopy imaging (HAADF-STEM) and their impact on the vortex-pinning parameters, determined in the microwave frequency range by a coplanar waveguide resonator (CPWR) technique. The films were irradiated with 1.15-GeV Pb ions, and the resulting columnar defects revealed a core-shell structure with an amorphous core surrounded by a strained crystalline shell. Statistical analysis (considering any cluster as an individual defect) yield a mean column radius of $r = 6\,\text{nm}$, which is in remarkable agreement with the radius of the confinement region obtained from fitting the irreversibility line within the Bose-glass model, $r_0 = 5.8\,\text{nm}$, providing strong experimental validation of the functional characterization through direct structural imaging. The core of the analysis lies in the determination of the main superconducting parameters (such as the penetration depth) and the vortex dynamics and pinning parameters – including the pinning constant, viscosity, depinning and crossover frequencies, creep factor, and pinning energy – through the CPWR microwave technique. These parameters are analyzed and discussed within the theoretical frameworks proposed by Gittleman–Rosenblum, Coffey–Clem, and Blatter et al. Overall, columnar defects were found to enhance the pinning efficiency and, consequently, the critical current density j_c and its ratio to the depairing current density, j_c/j_0. To determine their absolute values, a comparative analysis was carried out by combining results from the different experimental techniques with a theoretical treatment of j_c/j_0 as a function of the STEM-measured column radius. All results converge into a consistent framework, yielding $j_c(5\,\text{K}, 1\,\text{T}) = 8.8 \cdot 10^{11}\,\text{Am}^{-2}$ and $j_c/j_0 = 0.34$ for the YBCO films with irradiation-induced columnar defects.

1. Introduction

The investigation of $YBa_2Cu_3O_{7-\delta}$ (YBCO) films with columnar defects, as those induced by heavy ion irradiation, represents a paradigmatic case study, useful for testing vortex pinning models but also of practical relevance, e.g. for identifying critical current limits, thus providing a valuable reference also for other techniques used to introduce artificial defects in technological superconductors, in view of their application. In fact, in recent years particle irradiation has garnered significant attention as a controllable, flexible and effective method for material modification in the development of REBCO coated conductors ($REBa_2Cu_3O_{7-\delta}$, with RE = rare earth) for a number of demonstrative applications, including magnets, smart grids, MRI systems, and high-field scientific equipments [1].

It is well known that high-energy heavy ions produce in YBCO continuous defects along the ion track, provided that the electronic stopping power $(dE/dx)_e$ (the energy released by inelastic scattering to the electrons of the target) is higher than about 13–20 MeV/μm [2,3]. When this condition is fulfilled, columns of amorphized material are formed, with radii of the order of several nanometers [4], which revealed to be very efficient pinning centers [5]. In fact, columnar defects by heavy ion irradiation demonstrated to be effective pinning sites not only in cuprates [6], but also in other systems, e.g. iron-based superconductors [7–10].

* Corresponding author.
E-mail addresses: gianluca.ghigo@polito.it (G. Ghigo), mario.scuderi@cnr.it (M. Scuderi), michela.fracasso@polito.it (M. Fracasso), roberto.gerbaldo@polito.it (R. Gerbaldo), daniele.torsello@polito.it (D. Torsello), laura.gozzelino@polito.it (L. Gozzelino).

https://doi.org/10.1016/j.supcon.2026.100265
Received 6 March 2026; Received in revised form 12 May 2026; Accepted 20 May 2026
Available online 25 May 2026

Most of the vortex pinning studies concerned DC or low-frequency measurements that effectively probe, e.g., the depth of the pinning potential. On the other hand, in the microwave-frequency regime – due to very small vortex displacements – the bottom rather than the edge of the pinning potential is probed. Thus, these techniques are indeed complementary. Nonetheless, information about the height of the pinning potential well can be achieved also by studying the vortex creep contribution to the microwave complex resistivity.

Although the literature has addressed the use of microwave techniques to extract fundamental parameters, vortex pinning properties, and critical current density in YBCO films with irradiation-induced columnar defects, such studies have so far covered only limited aspects [11–15], and a systematic investigation combining direct structural characterization with microwave analysis is still lacking. The goal is integrating structural probes with comprehensive vortex-pinning analysis by microwave techniques in the very same samples, that could drive the research on ion-irradiated technological superconductors from an empirical approach to a mechanism-guided and defect-oriented design paradigm [1].

The aim of this paper is to achieve a consistent picture of the properties of YBCO films in the presence of columnar defects, through a correlative approach combining high-resolution HAADF-STEM imaging (High-Angle Annular Dark Field - Scanning Transmission Electron Microscopy), microwave analysis, DC measurements, and theoretical models. The paper is organized as follows. Section 2 deals with the experimental details, and Section 3 is about the characterization of pristine YBCO films by the microwave CPWR technique, to extract the London penetration depth $\lambda_L(T)$. An extended HAADF-STEM analysis of the columnar defects introduced by heavy-ion irradiation in YBCO is reported in Section 4, providing direct visualization of the core-shell defect structure and a comprehensive statistical analysis resulting in an estimation of the mean column radius. In Section 5, the irreversibility line of irradiated YBCO obtained by DC measurements is analyzed with the aim to estimate the radius of the vortex confinement region, to be compared with the column radius. In Section 6, the vortex dynamics and pinning parameters are derived and discussed. In particular, in Section 6.1 the Gittleman-Rosenblum approach is used to obtain the depinning frequency ν_p, the vortex viscosity η and pinning constant k_p, as a function of temperature and magnetic field. In Section 6.2, $k_p(T)$ is used to conclude that the pinning in pristine YBCO is of δl type, through the Blatter et al. model. In Section 6.3, the creep factor χ and the normalized pinning energy barrier u are obtained from multifrequency measurements within the Coffey-Clem model, and finally in Section 6.4 the effects of the introduction of columnar defects on the above mentioned parameters is shown and discussed. Section 7 deals with the ratio between the critical current density and the depairing current density, j_c/j_0, in irradiated YBCO, comparing the experimental results (Section 7.1) to theoretical estimations (Section 7.2). Finally, in Section 8 we summarize the results from the different characterization techniques and by a comparative analysis we demonstrate their consistency and determine the last remaining unknown quantities, i.e. the coherence length, and consequently the critical current density and the j_c/j_0 ratio for the YBCO film with irradiation-induced columnar defects. Concluding remarks are given in Section 9.

2. The experiment

The 250-nm-thick $YBa_2Cu_3O_{7-\delta}$ (YBCO) films – grown by reactive thermal co-evaporation on MgO substrates – were acquired by CERACO ceramic coating GmbH (M type films) [16]. The coplanar waveguide resonators for the microwave characterization and the Hall bars for DC resistivity measurements were obtained by standard photolithographic process followed by wet etching of the YBCO films.

A standard four-probes technique (with bias current polarity inversion and measurement averaging) was used to measure the DC resistivity vs. temperature at several applied field. The critical temperature of the pristine films is $T_c = 87.5\,\mathrm{K}$ and their normal state resistivity is $\rho_n = 65\,\mu\Omega\,\mathrm{cm}$.

The microwave characterization is based on the measurement of the complex transmission coefficient S_{21} (ratio of the transmitted voltage to the incident voltage) of half-wavelength coplanar waveguide resonators (CPWRs) as a function of frequency (resonance curve), by means of a vector network analyzer. Resonance curves were measured at about 7.95 GHz for different values of temperature and DC magnetic field, applied perpendicular to the film plane [17]. For a CPWR, we also measured the first harmonic resonance curves, at about 15.8 GHz, to allow a multifrequency analysis that could corroborate the results and provide additional insight.

The devices were irradiated at room temperature and in vacuum with a 1.15-GeV Pb ion beam at the PIAVE-ALPI facility of the INFN Laboratori Nazionali di Legnaro, Italy, up to a fluence of $\phi = 1.5 \cdot 10^{11}\,\mathrm{cm}^{-2}$, corresponding to a dose equivalent field (the magnetic field ideally needed to fill each ion track with a flux line) of $B_\phi = 3\,\mathrm{T}$. Ions were directed perpendicular to the film plane and implanted into the substrate at a depth of 39.0 μm, as calculated by means of the Monte Carlo code SRIM [18]. The same code gives, for the electronic stopping power, $(dE/dx)_e = 45\,\mathrm{MeV/\mu m}$, definitely above the threshold for the formation of continuous defects along the ion track. After irradiation, T_c decreased by about 1 K and the normal state resistivity enhanced to $101\,\mu\Omega\,\mathrm{cm}$.

An extensive Transmission Electron Microscopy (TEM) analysis was performed on plan-view TEM specimen prepared from the irradiated YBCO films using standard thinning procedures. The structural characterization was performed on a JEOL JEM-ARM200CF operated in scanning TEM (STEM) mode and using high-angle annular dark field (HAADF) imaging to visualize ion-induced damage.

3. Pristine film: London penetration depth

The resonance curves of the CPWR for the fundamental mode at $f \approx 7.95\,\mathrm{GHz}$ and for the first harmonic mode at $f \approx 15.8\,\mathrm{GHz}$ were measured (Fig. 1(A)) and fitted by a Lorentzian function [17], allowing the determination of the resonance frequency and the unloaded quality factor. The analysis of such parameters enables the determination of the absolute value of the London penetration depth, λ_L, as previously described in detail [17]. Fig. 1(C) shows the temperature dependence of λ_L, obtained by fitting the normalized resonance frequency for both the fundamental and first harmonic modes (examples in Fig. 1(B)). The fitting procedure was performed over a limited temperature range using the general parametric expression

$$\lambda_L(T) = \lambda_L(0)/\sqrt{1 - (T/T_c)^\gamma} \tag{1}$$

where $\lambda_L(0)$, T_c and γ were treated as free fitting parameters. The values of $\lambda_L(T)$ were then recalculated over the entire temperature range by interpolating and extrapolating the substrate permittivity, $\varepsilon_r(T)$ [17]. From the fit, a value of $\gamma = 2.1$ was obtained for both the modes, consistent with reports in the literature for YBCO [19]. As expected, the analysis of the two modes at different frequencies gives virtually the same $\lambda_L(T)$ curve (Fig. 1(C)). In this geometry, the obtained penetration depth practically coincides with the in-plane $\lambda_{L,ab}$.

4. HR-STEM analysis of columnar defects

4.1. STEM imaging

HAADF-STEM imaging provides Z-contrast dominated by high-angle Rutherford-like scattering, with intensity scaling approximately as Z^2 [20]. Heavy-ion irradiation in crystalline YBCO produces amorphous columnar defects [2] that suppress channeling, altering the scattering distribution [21]. Although dechanneling would nominally increase HAADF intensity, the amorphous tracks exhibit a reduced atomic density, lowering the number of scattering centers. This effect dominates,

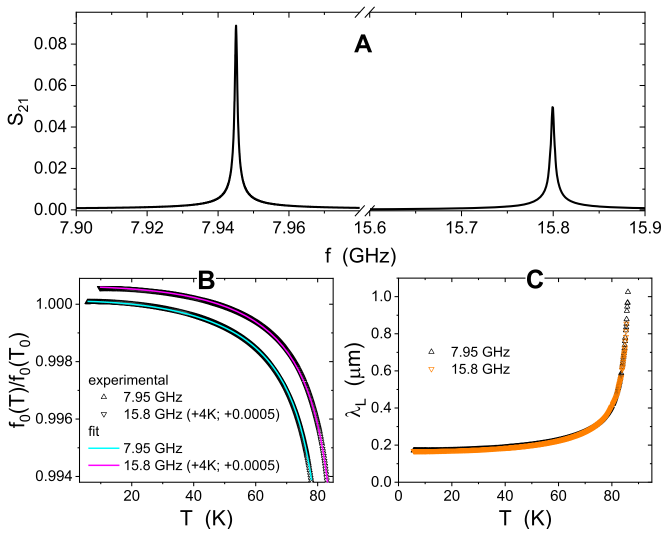

Fig. 1. (**A**) CPWR resonance curves (magnitude of S_{21} vs. frequency) at T = 5.8 K for the fundamental (left) and the first harmonic mode (right). (**B**) Examples of the normalized resonance frequency fit. The first harmonic curves at 15.8 GHz were shifted by 4 K horizontal and 0.0005 vertical, for the sake of clarity. (**C**) London penetration depth as a function of temperature, obtained by fitting data for both the fundamental and first harmonic modes.

yielding a net decrease in HAADF contrast. As a result, ion-track columns appear darker than the surrounding crystalline matrix, enabling their direct visualization in irradiated superconducting films.

Fig. 2(A) shows a representative plan-view STEM Z-contrast image of an irradiated YBCO film. The columnar defects are clearly visible as darker circular features against the brighter crystalline matrix. A closer examination of the track morphology reveals a more complex contrast profile than a simple dark region, indeed the effects of the columnar defects extend further into the crystalline matrix. Fig. 2(B) presents a higher-magnification image of an individual columnar track, accompanied by an intensity line profile measured across the track diameter shown in Fig. 2(C). The line profile reveals three distinct regions: (i) a central dark-contrast core corresponding to the *fully amorphized* material along the ion trajectory, where the crystalline structure was completely disrupted by the energy deposition during ion passage; (ii) an intermediate region surrounding the amorphous core, exhibiting a brighter contrast compared to the crystalline matrix, which corresponds to a strained and *defected* crystalline shell where the lattice was perturbed but not fully amorphized; and (iii) the *unperturbed* crystalline matrix. This core-shell structure reflects the radial distribution of damage induced by the ion impact [22,23]: the core experiences complete structural collapse, while the surrounding shell undergoes elastic deformation due to point-defect accumulation and local oxygen reordering [3]. For the purpose of vortex pinning analysis, it is physically meaningful to include both the amorphous core and the damaged crystalline shell in the effective defect diameter, as both regions contribute to the pinning potential experienced by flux lines. Therefore, in the diameter measurements reported in Section 4.3, we adopted the criterion indicated in Fig. 2(C) that extends the defect diameter beyond the darkest central region to encompass the full extent of the contrast variation, thereby accounting for the complete damaged zone that acts as an effective pinning center.

Fig. 2(A) also highlights a key aspect of track counting: some columnar tracks appear as isolated defects, whereas others are partially overlapping. While such features originate from the stochastic nature of ion irradiation and must be counted as distinct events when determining the experimental fluence (Section 4.2), they effectively act as a single, wider defect in shaping the pinning landscape (Section 4.3).

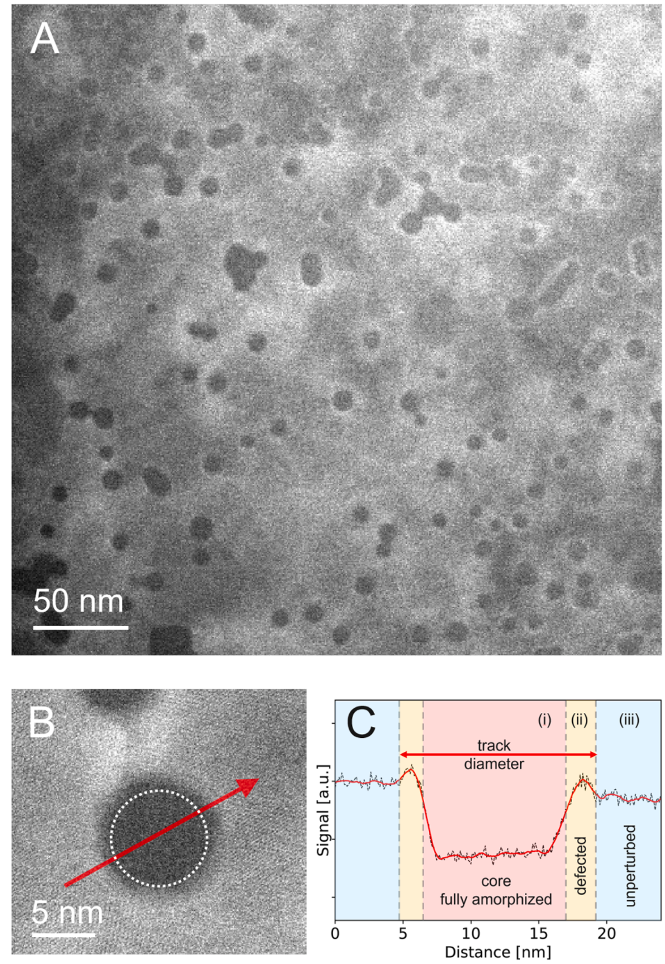

Fig. 2. (**A**) Plan-view HAADF-STEM image of irradiated YBCO showing the columnar tracks as darker circular features. (**B**) Higher-magnification STEM image of a track (white dashed circle) with intensity line profile measured across the track diameter (red arrow). (**C**) Line scan profile that reveals the contrast gradient from the amorphous core (dark) through the strained crystalline shell (bright) to the pristine matrix (intermediate).

4.2. Quantitative track analysis

Individual ion tracks were systematically counted over multiple STEM images covering a statistically significant area. Two counting methodologies were employed: (i) for fluence verification, each individual ion impact was counted independently, including those forming overlapping clusters (as each represents a distinct implantation event); (ii) for pinning analysis, clustered tracks were treated as single effective defects, since from the vortex perspective they act as unified pinning centers rather than independent sites.

The experimentally determined fluence, obtained by counting all individual ion impacts, yielded ϕ_{exp} = 1.46 × 10^{11} cm^{-2}, in excellent agreement with the nominal implantation fluence ϕ_{nom} = 1.5 × 10^{11} cm^{-2}. This validates the STEM imaging approach and confirms the uniformity of the irradiation process and the validity of the experimental protocol for the control of the fluence during ion irradiation. A similar result was obtained also on iron-based superconductors irradiated with 1.2 GeV Pb ions [24].

For the pinning analysis, the second counting procedure (point ii) was employed. This approach yields an effective column density reduced to about 85% of the nominal fluence. Consequently, the effective pinning landscape experienced by vortices is characterized by a lower density of pinning centers, each with an increased effective size, consistent with the diameter distribution that will be discussed in Section 4.3, as it more accurately captures the number and spatial distribution of independent pinning sites available for vortex trapping.

4.3. Diameter distribution analysis

In the context of vortex pinning, we analyze the ion-track diameter distribution, which includes both isolated and clustered tracks formed by a partial overlap of ion impacts. As clustered tracks behave as single effective pinning centers, the measured distribution reflects the effective defect size relevant for pinning.

Track diameter measurements were performed on multiple STEM images to ensure adequate statistical significance. The empirical probability density function was estimated using kernel density estimation (KDE) with a Gaussian kernel [25], adopting Scott's rule for bandwidth selection [26] (Fig. 3). This non-parametric approach enables visualization of the diameter distribution without imposing any a priori assumption on its functional form. For visualization purposes only, histograms were constructed using the Freedman–Diaconis rule [27] for optimal bin width selection; however, all statistical parameters were extracted from unbinned data to avoid discretization artifacts.

Statistical analysis revealed that approximately 34% of all individual tracks participate in clustering events. Although these clustered tracks contribute to the upper tail of the diameter distribution, the majority of tracks remain isolated, forming a dominant unimodal population. These features indicate deviations from a purely single-population distribution and reflect the contribution of merged or partially overlapping tracks.

Despite these deviations, a single log-normal distribution was adopted to describe the diameter data. This choice is physically motivated by the multiplicative cascade of stochastic processes governing thermal spike formation, including electronic energy deposition, radial energy diffusion, and rapid quenching [28,29], and is further supported by the observation that clustered tracks do not form a distinct secondary population. Moreover, the log-normal model provides a robust description of the dominant unimodal component of the distribution, with clustered tracks contributing primarily to the upper tail rather than forming a fully distinct secondary peak.

Fig. 3 shows the resulting diameter distribution of the amorphous columnar defects. From the log-normal fit, a mean track diameter of (12 ± 4) nm was obtained, corresponding to a mean radius of $r = (6 \pm 2)$ nm. This value represents the effective pinning center size, accounting for both isolated ion tracks and clustered configurations treated as single pinning objects. As a comparison, 1.4 GeV Pb ions were found to produce in YBCO coated conductors amorphous columnar tracks with a radius of (5.4 ± 0.6) nm, surrounded by a region where the amount of O and Cu is decreased, over a length of ~ 3 nm [3]. Using the mean effective diameter d = 12 nm, the fractional coverage, i.e. the fraction of amorphized area, can be calculated as $F_{coverage} = \phi \times \pi r^2 = 1.5 \times 10^{11}\ \text{cm}^{-2} \times \pi \times (6 \times 10^{-7}\ \text{cm})^2 \approx 0.17$ (17%), indicating operation in the dilute overlapping regime where track-track interactions are present but do not dominate the microstructure [30].

5. Irreversibility line

In the temperature vs. magnetic field phase diagram, the irreversibility line (IL) is the line above which the depinning critical current drops to zero. It was determined from DC measurements as the temperature T_{irr} at which the resistivity equals 10% of the normal-state value, and it is shown in Fig. 4 for the same Hall bar before and after irradiation, in terms of reduced temperature $t = T_{irr}/T_c$. The IL of the pristine film is smooth, while after irradiation a characteristic kink shows up (indicated by an arrow in the graph), which is assumed to separate a low-field regime, where single vortex pinning by columnar defects occurs, from a collective pinning regime at higher fields [5]. It should be noted that the IL kink occurs at an accommodation field $B^* = 2.35\,\text{T} = 0.78\,B_\phi$, which

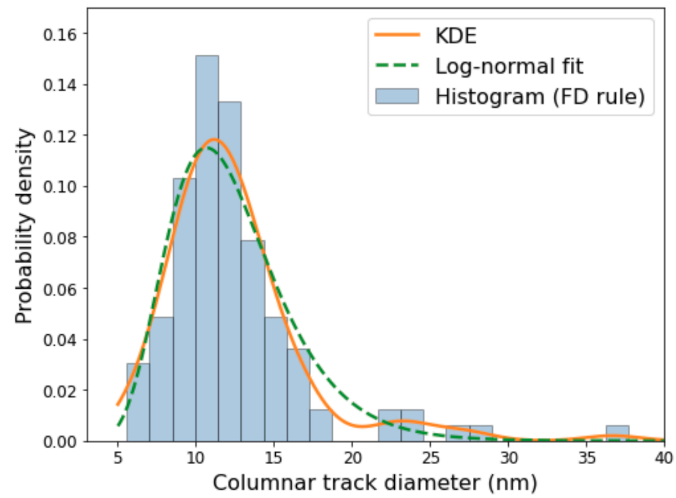

Fig. 3. Diameter distribution of columnar defects induced by 1.15 GeV Pb ions in YBCO. The empirical distribution is shown as a kernel density estimation (solid line), with the histogram reported as a visual guide. The log-normal fit (dashed line) describes the data, accounting for both isolated tracks and clustered configurations. The mean effective track diameter is 12 ± 4 nm.

is lower than the dose equivalent field mainly due to clustering and partial overlap of the randomly distributed columnar tracks. In fact, this accommodation field matches the effective column density calculated by treating clustered tracks as single defects from the STEM images in Section 4.2 point (ii), where the effective column density was estimated as 85% of the nominal fluence. Therefore, we use B^* to estimate the average distance between the effective columns $a = \sqrt{\Phi_0/B^*} = 29.7$ nm, which is useful for the following analysis.

According to the standard analysis based on the Bose-glass analogy [31], it is possible to fit the low-field part of the IL after irradiation (considered as normalized irreversibility temperature as a function of field, $t_{\rm BG}(H)$) starting from the IL before irradiation, assumed to be a good approximation of the vortex melting line, $t_{\rm m}(H)$. It turns out that [31,32]:

$$t_{BG}(H) = \frac{t_m(H) + \gamma\, t_{on}}{1+\gamma}, \tag{2}$$

where t_{on} is the maximum reduced temperature at which the columns are effective pinning centers. The fit is done with t_{on} and γ as fitting parameters and it is shown in Fig. 4 as a solid orange line. The parameter γ is a function of the radius of the vortex confinement region, r_0

$$\gamma = \frac{r_0^2}{4a\xi\sqrt{Gi}},$$

where the Ginzburg number Gi in turn can be expressed as [33]

$$Gi = \frac{1}{2}\left(\frac{2\pi\mu_0 k_B T_c \Gamma \lambda_{ab}^2}{\xi \Phi_0^2}\right)^2,$$

and Γ is the anisotropy factor. The radius of the vortex confinement region finally reads

$$r_0 = \sqrt{\frac{4\sqrt{2}a\pi\mu_0 k_B T_c \Gamma \lambda_{ab}^2 \gamma}{\Phi_0^2}}. \tag{3}$$

If we assume, according to literature [34], $\Gamma = 5$, and use the values of T_c, λ_{ab} and γ from the experiment, we obtain $r_0 = 5.8$ nm, that is in remarkable agreement with the radius of the columnar defects estimated by HRTEM analysis in Section 4.3, $r = (6 \pm 2)$ nm [35].

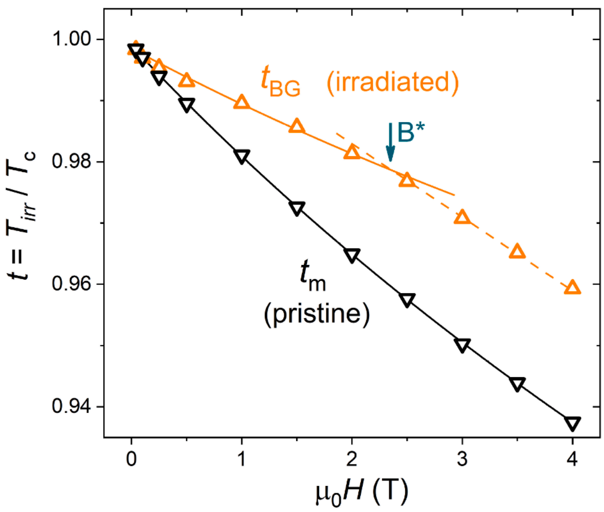

Fig. 4. The irreversibility line for the same YBCO Hall bar before (black symbols) and after irradiation (orange symbols), in terms of the irreversibility reduced temperature $t = T_{irr}/T_c$ as a function of the applied magnetic field. Interpolated pristine data are assumed to approximate the melting line t_m (black line), while the fit of the low-field data after irradiation according to Eq. (2) is reported as a solid orange curve, t_{BG} (fitting parameters: $\gamma = 1.06$, $t_{on} = 0.997$). The dashed line is a guide to the eye, and the arrow marks the kink separating the two vortex pinning regimes at the accommodation field B^*, discussed in the main text.

6. Vortex dynamics and pinning parameters

The vortex dynamics and pinning parameters are deduced from the experiment through the comparison between microwave CPWR measurements with and without applied DC magnetic field, allowing us to determine the complex resistivity term ρ_{vm} accounting for the vortex motion contribution to dissipation [36]. The way ρ_{vm} is connected to the vortex parameters depends on the adopted model for the high-frequency response of the vortex matter. Below, we consider two different approaches to analyze our experimental ρ_{vm} data, the Gittleman-Rosenblum (GR) model and the Coffey-Clem (CC) model. Although both involve simplifying assumptions, their reference parameters prove to be extremely useful for studying the impact of introducing artificial pinning centers on vortex dynamics.

6.1. Vortex parameters by the Gittleman-Rosenblum model

In its simplest approach, neglecting thermal-fluctuation-induced creep, strong vortex bending and collective effects, the high frequency vortex motion response is determined by a pinning force and a drag force, opposing to the Lorentz force exerted on the vortex. The high frequency regime imposes to vortices very small oscillations around equilibrium positions. In the approximation of harmonic oscillations, the pinning force can simply be written as $k_p\mathbf{u}$, where $\mathbf{u}$ is the displacement and k_p is the pinning constant. The dissipation due to the motion of vortices, related to the relaxation processes of the quasiparticles in the core, is accounted for as a drag force $\eta\mathbf{v}$, where $\mathbf{v}$ is the vortex velocity and η the vortex viscosity. Finally, a key parameter is the depinning frequency, that is a combination of the previous ones, $\nu_p = k_p/\eta$, representing the limit below which elastic motion occurs, and above which a purely dissipative motion dominates.

Within this framework, the vortex parameters can be estimated by the Gittleman-Rosenblum (GR) model [37], giving the complex resistivity term that is needed to account for vortex motion as

$$\rho_{vm} = \frac{\rho_{ff}}{1 - i\,\nu_p/\nu} \tag{4}$$

where $\rho_{ff} = \Phi_0 B/\eta$ is the flux flow resistivity. The practical way to obtain k_p, η and ν_p directly from CPWR measurements was described in detail in Refs. [36,38]. To this aim, the knowledge of the absolute values of the London penetration depth, discussed in Section 3, is needed.

In Fig. 5(A) ν_p is reported for two measurement frequencies of 7.95 GHz (fundamental mode) and 15.8 GHz (first harmonic) as a function of magnetic field, for $T = 5.8$ K. It is clear that ν_p is significantly different for the two measurement frequencies: this could be ascribed to a flux creep effect that in the GR model is neglected. To address this issue, a CC analysis is reported in Section 6.3 below, showing that in fact flux creep is not negligible even at low temperatures. Although it is extremely low, it is enough to explain the observed $\nu_p(\nu)$.

The other independent parameter that can be estimated by the GR analysis is the pinning constant k_p, shown in Fig. 5(B) and (C) as a function of field and temperature, respectively. In this paper, the pinning constant is used with two main aims: (i) $k_p(T)$ for pristine YBCO films is used to distinguish between δl and δT_c type pinning, to characterize the pinning landscape before ion irradiation (see Section 6.2); (ii) $k_p(H)$ at low temperatures is used to determine the critical current density j_c and its ratio to the depairing current j_0 for YBCO films with columnar defects (see Section 7.1).

6.2. δl-type pinning within the Blatter et al. model

The $k_p(T)$ curves obtained by the CPWR technique as described above (Fig. 5(C)), spanning over several orders of magnitude, are suitable to check the validity of the collective pinning model proposed in the review of Blatter et al. [39] and to investigate whether pinning in the pristine YBCO films is of δl- or δT_c-type. In fact, in type II superconductors pinning results from spatial variations of different coefficients of the Ginzburg-Landau free-energy functional, associated with disorder in the transition temperature T_c, and/or from spatial modulation of the charge carrier mean free path l near lattice defects [39]. In particular, it has been shown that [40] $k_p(t) = \mu_0 H_c^2 \delta^{2/3} \sim H_{c1} H_{c2} \delta^{2/3} \sim \lambda_L(t)^{-2} H_{c2}(t)\delta^{2/3}(t)$, where t is the reduced temperature and δ is a dimensionless parameter, with different temperature dependencies in the case of δl-type pinning, $\delta \sim (1-t)^{3/2}$, and δT_c-type pinning, $\delta \sim (1-t)^{-1/2}$. For the penetration depth, we used the temperature dependence deduced for the same resonators in Section 3, $\sim (1-t^{2.1})^{-1/2}$, and for the upper critical field the phenomenological expression $\sim (1-t^2)$. Thus, finally we get $k_p(t) \sim (1-t^{2.1})(1-t^2)(1-t)$ for δl-type pinning, and $k_p(t) \sim (1-t^{2.1})(1-t^2)(1-t)^{-1/3}$ for δT_c-type pinning. Fig. 5(C) shows that the experimental data are very well described within the δl scenario, i.e. with a model of single vortices pinned by randomly distributed weak pinning centers via spatial fluctuations of the charge carrier mean free path, in agreement with the results obtained in Ref[41]. by analyzing the critical current density.

6.3. Creep factor and pinning energy by the Coffey-Clem model

The improvement of the Coffey-Clem (CC) model [42] with respect to the GR one is that it includes the effects of thermal fluctuations, resulting in vortex creep motion. On the other hand, its simplification is the assumption of a sinusoidal pinning potential. Within this model, the vortex motion resistivity is given by

$$\rho_{vm} = \rho_{ff}\frac{\chi + i\nu/\nu_c}{1 + i\nu/\nu_c} \tag{5}$$

where $\rho_{ff} = \Phi_0 B/\eta$ as in the GR model, χ is a creep factor ($0 \le \chi \le 1$), and ν_c is the crossover frequency, that has a physical meaning similar to ν_p in the GR model. In fact, in the limit of $\chi \to 0$, $\nu_c \to \nu_p$. The creep factor is a function of the normalized energy barrier height $u = U_0/k_BT$, being U_0 the height of the pinning potential and k_B the Boltzmann constant:

$$\chi = \frac{1}{\left[I_0\left(\frac{u}{2}\right)\right]^2} \tag{6}$$

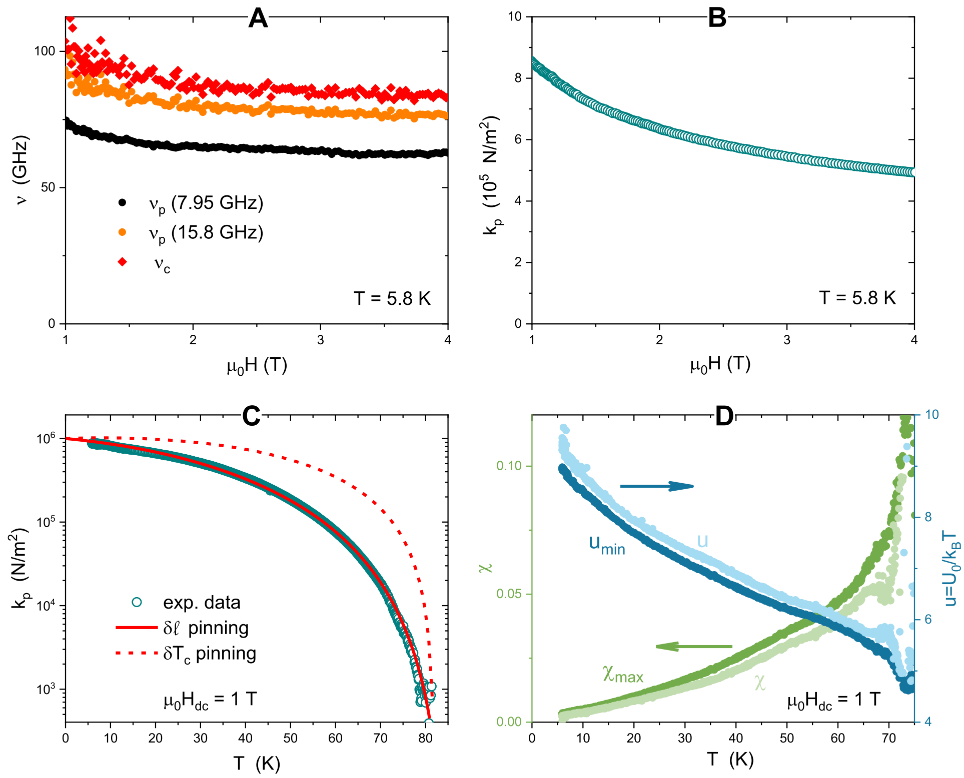

Fig. 5. Pinning parameters for the pristine films: (**A**) field dependence of the depinning frequency ν_p, as deduced by the GR analysis from measurements at two different frequencies (see main text at Section 6.1), and of the crossover frequency ν_c, from the CC analysis (Section 6.3). (**B**) Field dependence of the pinning constant, k_p. (**C**) Temperature dependence of the pinning constant for an applied field of 1 T, fitted by the δl pinning mechanism equation (solid line; the dotted line is the behavior expected for the δT_c-type pinning, see Section 6.2). (**D**) Temperature dependence of the creep factor χ and its maximum value $\chi_{\max}$ (left) and of the normalized energy barrier height u and its minimum value $u_{\min}$ (right), see the discussion in Section 6.3.

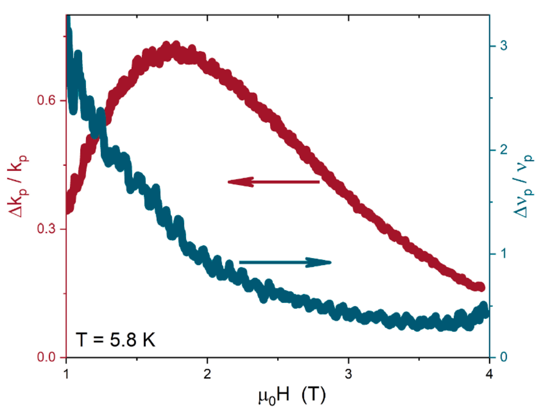

Fig. 6. Relative increase of the pinning constant (left) and depinning frequency (right) for the same CPWR after irradiation, as a function of the applied magnetic field.

where I_0 is the modified Bessel function of the first kind of order zero.

The parameters in Eq. (5) can be obtained by a multi-frequency analysis. We used the fundamental and the first harmonic signals of the CPWR to obtain the real and imaginary parts of the vortex motion resistivity at two different frequencies. Therefore, through Eq. (5), we have four equations allowing us to determine the three unknown ρ_{ff}, χ, and ν_c. Then, by reversing Eq. (6), we get the normalized energy barrier u. An example is given in Fig. 5(D), where $\chi(T)$ and $u(T)$ for an applied field of 1 T are shown, and in Fig. 5(A), where the crossover frequency is reported. The normalized energy barrier turns out to be in good agreement with other microwave analyses: for example, Powell et al. reported, for YBCO films at microwave frequencies, $u(10\text{K}) = 7$ and $u(60\text{K}) = 4.4$ [43], close to our estimate. However, all these values are significantly lower than those estimated by other methods, e.g. $u \sim 25$ at low temperatures from relaxation of magnetization in YBCO single crystals [44]: the reason for this discrepancy could be ascribed to different conditions in terms of probing currents and vortex displacements in relation to the shape of the pinning potential well, but is in fact currently unclear and deserves further investigation.

When multi-frequency measurements are not available, a discussion about creep factor and energy barrier is still possible, in terms of their maximum and minimum values, respectively. In fact, in order to preserve the physical meaning of ν_c, that must be a real quantity, a constraint on χ emerges by considering Eq. (5), as previously reported in Ref. [45]. This gives an upper limit for the creep factor, $\chi_{\max}$, implying a lower limit for the normalized energy barrier height, $u_{\min}$. These values can be calculated directly from the data of single-mode measurements, and are reported in Fig. 5(D). It is clearly shown that $\chi_{\max}(T)$ and $u_{\min}(T)$ have the same temperature dependence as $\chi(T)$ and $u(T)$ estimated by the multi-frequency analysis and are very close to them, therefore a discussion about the effects of columnar defects on $\chi_{\max}(T)$ and $u_{\min}(T)$ – reported in the next subsection – seems fully meaningful.

6.4. *Effects of the columnar defects on the pinning parameters*

The effects of the introduction of columnar defects by ion irradiation on $k_p(H)$, $\nu_p(H)$, $\chi_{\max}(T,H)$ and $u_{\min}(T,H)$ is shown in Figs. 6–7, where data from the same CPWR before and after irradiation are compared. In particular, in Fig. 6 the relative increments of the pinning constant (left) and the depinning frequency (right) after irradiation are reported.

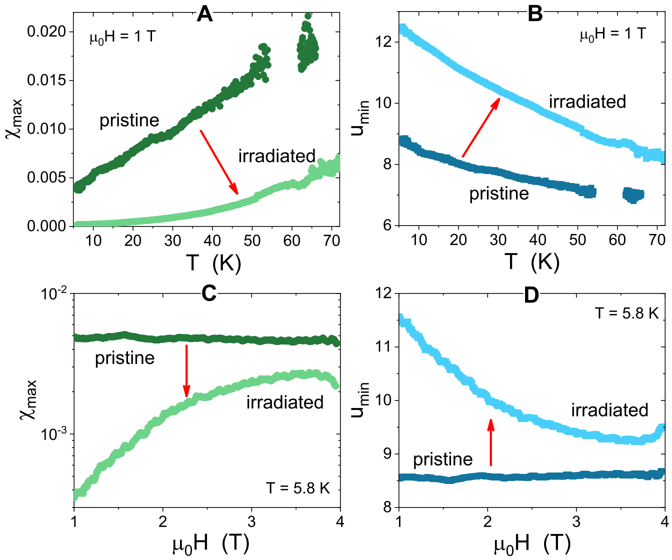

Fig. 7. Maximum creep factor χ_{max} before and after irradiation, as a function of temperature (**A**) and field (**C**). Minimum normalized height of the pinning potential u_{min} before and after irradiation, as a function of temperature (**B**) and field (**D**). Red arrows indicate the shift of the curves after irradiation.

The maximum increment of the pinning constant is for a field of about 1.75 T, slightly lower than the accommodation field B^*. In Fig. 7(A) it is clearly shown that for fields below the dose equivalent field and the accommodation field, $\chi_{max}(T)$ is much lower after irradiation and with a lower slope as a function of temperature. Consequently, $u_{min}(T)$ increases (Fig. 7(B)). The same trend is shown by $\chi_{max}(H)$ and $u_{min}(H)$ in Fig. 7(C)-(D), for $T = 5.8$ K. The improvement is higher for fields lower than the accommodation field, where single vortex pinning by columns is expected.

7. The critical/depairing current density ratio

7.1. Experimental determination of the j_c/j_0 ratio

The critical current density j_c is obtained from the pinning constant, as determined in Section 6.1, through [46] $j_c = k_p\xi/\Phi_0$, while the depairing current density is deduced within the Ginzburg-Landau theory as $j_0 = \Phi_0/(3^{3/2}\pi\mu_0\lambda_L^2\xi)$ [47]. Therefore, their ratio is

$$\frac{j_c}{j_0} = \frac{3^{3/2}\pi\mu_0\lambda_L^2\xi^2 k_p}{\Phi_0^2} \tag{7}$$

In Eq. (7), the only quantity that we can not directly infer from our data is the coherence length. For example, if we assume for ξ the reference values of 1.0 nm or 1.15 nm, the $j_c/j_0(H)$ curves at low temperature for the irradiated YBCO CPWR are the ones shown in Fig. 8 (the reason for the choice of $\xi = 1.15$ nm is clarified later in the text, see Section 8). Data show a saturation at lower fields (indicated by the horizontal green lines in the graph), while the $\sim 1/H$ behavior expected for the collective regime show up at higher fields (red curves).

7.2. Theoretical determination of the j_c/j_0 ratio

In the limits of very small or very large defects, i.e. for the radius of the columnar defect r very small or very large with respect to ξ, the pinning potential has been calculated by Blatter et al. (see Eqs.(9.55) and (9.59) in Ref. [39]. However, in the case of irradiation-induced columnar defects, the most frequent situation is in between. This case was studied by Klaassen et al. [48], who derived, within the same theoretical framework, a general expression for the pinning potential per unit

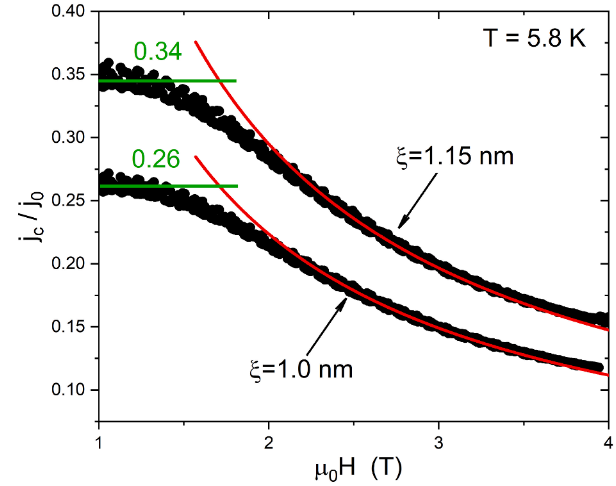

Fig. 8. Experimental j_c/j_0 (ratio between the critical current density and the depairing current density) for the irradiated CPWR as a function of the applied field, for $T = 5.8$ K and for two different values assumed for the coherence length ξ: 1 nm and 1.15 nm. At lower fields, the saturation of the ratio to an about constant value is indicated by the horizontal green lines, while the $\sim 1/H$ behavior expected for the collective regime at higher fields is indicated by red curves.

length, valid also when the column radius is comparable to the coherence length, i.e. for $r \approx \sqrt{2}\xi$:

$$\varepsilon_r(R) = -\frac{\varepsilon_0}{2}\left[\operatorname{arcsinh}\left(\frac{r^2 - R^2 + 2\xi^2}{2\sqrt{2}\xi|R|}\right) - \operatorname{arcsinh}\left(\frac{-R^2 + 2\xi^2}{2\sqrt{2}\xi|R|}\right)\right]$$

where R is the distance of the vortex from the center of the pinning site and $\varepsilon_0 = \Phi_0^2/(4\pi\mu_0\lambda^2)$ is a reference value for the vortex energy per unit length. Then, the maximum pinning force can be calculated as $f_{p,max} = -d\varepsilon_r/dR|_{max} \approx -d\varepsilon_r/dR|_{R=r}$ and finally the critical current density, normalized to the depairing current density, is obtained by equating the maximum pinning force to the Lorentz force. It reads [48]

$$\frac{j_c}{j_0} = \frac{3\sqrt{3}}{8}\left(\frac{r^2+\xi^2}{r\sqrt{2r^2+\xi^2}} - \frac{\xi}{r}\right) \tag{8}$$

8. Pinning by columnar defects: A comparative analysis

Now, we can check whether all the pieces of information described and discussed in the previous Sections about pinning by columnar defects compose a consistent and comprehensive picture. In Fig. 9, the j_c/j_0 vs. ξ curves obtained experimentally by Eq. (7) and theoretically by Eq. (8) are compared. In the latter, the column radius was assumed to be $r = 5.8$ nm according to the HRTEM and IL analyses. It turns out that the two approaches are consistent, i.e. they give the same ratio $j_c/j_0 = 0.34$, if $\xi = 1.15$ nm, which is a value fully reasonable for the coherence length of irradiated YBCO. This is deduced from the intersection of the two main curves in Fig. 9 (marked by a black circle). By considering the uncertainty in the determination of the column radius from STEM analysis (± 2 nm) and the estimated errors for λ_L and k_p (± 10 nm and $\pm 10^5$ N/m^2, respectively, giving about $\pm 12\%$ error for the current density ratio in Eq. (7)) the colored regions in the graph can be drawn, resulting in the evaluation of the (asymmetric) errors for j_c/j_0 and ξ: $j_c/j_0 = 0.34^{+0.03}_{-0.05}$ and $\xi = \left(1.15^{+0.11}_{-0.12}\right)$ nm.

In literature, different values are reported for ξ in YBCO films, ranging from 1.18 nm to 2.5 nm [49,50]. Our estimation seems consistent (within the errors) with the lower limit. It should be also noted that in the dirty limit, when the electron mean free path becomes lower than the intrinsic coherence length ξ_0, the effective coherence length ξ is modified due to impurity scattering, resulting in a reduced value with respect to ξ_0. Therefore, a slightly smaller value for ξ can be reasonably

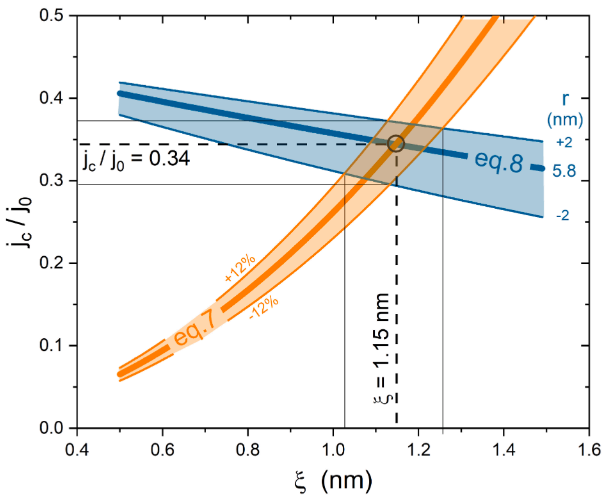

Fig. 9. Comparison between the curves critical/depairing current ratio j_c/j_0 vs. coherence length ξ as deduced at $T = 5.8\,\mathrm{K}$ experimentally by means of Eq. (7) (orange thick line) and theoretically by means of Eq. (8) (blue thick line), assuming for the radius of the columnar defects $r = 5.8\,\mathrm{nm}$ according to the IL and STEM analyses. For the consistency of the overall results, the values of $\xi = 1.15\,\mathrm{nm}$ and $j_c/j_0 = 0.34$ are deduced from the intersection of the two curves (marked by a black circle). The blue area corresponds to solutions of Eq. (8) for values of r within the error estimated by the STEM analysis, i.e. $\pm 2\,\mathrm{nm}$. The orange area corresponds to indetermination of $\pm 12\%$ in the values given by Eq. (7), stemming from estimated errors in λ_L and k_p. The intersection of the colored areas gives the (asymmetric) maximum errors for j_c/j_0 and ξ (thin black lines), reported in the main text.

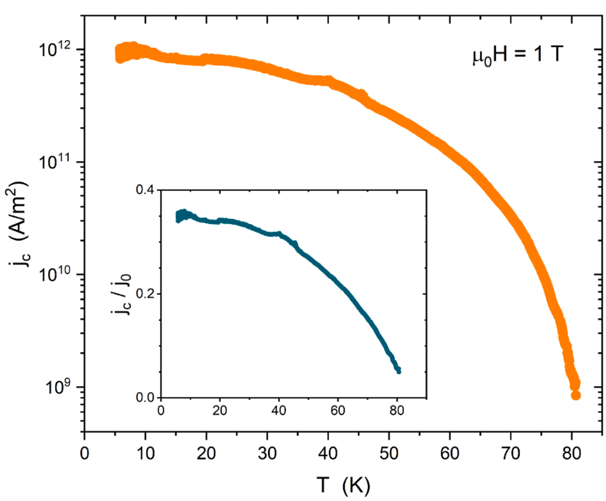

Fig. 10. Critical current density as a function of temperature, evaluated for $\mu_0 H = 1\,\mathrm{T}$ by the method described in the text. The inset shows the corresponding critical current to depairing current density ratio, as a function of temperature.

expected in irradiated samples, due to the introduced disorder. In conclusion, since our estimation of ξ is in fact in accordance with literature, we state that overall the complete set of results shows self-consistency.

After the coherence length being assessed, the absolute value of the critical current density can be estimated as $j_c(5\,\mathrm{K}, 1\,\mathrm{T}) = (8.8 \pm 1.0) \cdot 10^{11}\,\mathrm{Am^{-2}}$. The same procedure shown in Fig. 9 for data at T = 5.8 K can be extended to the whole temperature window, which could be of greater practical significance for engineering applications. By equating Eqs. (7) and (8), with $\lambda = \lambda(T)$ and $k_p = k_p(T)$ from the microwave analysis and $r = 5.8\,\mathrm{nm}$ from IL and STEM, we get the $j_c(T)$ and $j_c/j_0(T)$ curves shown in Fig. 10, both for the magnetic field of 1 T. A comparison with literature data for $j_c(T, \mu_0 H = 1\,\mathrm{T})$ in YBCO films [48,51–59] – although we used a different, indirect method – suggests that our samples with columnar defects exhibit strong performance across the entire temperature range.

9. Concluding remarks

This work systematically investigates all aspects related to the production and characterization of columnar defects in YBCO via heavy-ion irradiation, as well as their impact on vortex-pinning parameters, determined in the high-frequency regime using the CPWR microwave technique. The correlative approach establishes a comprehensive and self-consistent framework for understanding vortex pinning by engineered columnar defects.

In detail, YBCO thin films were irradiated with 1.15 GeV Pb ions, and the resulting columnar defects were examined by extensive plan-view HAADF-STEM analysis. The Z-contrast imaging directly visualized the amorphous columnar tracks as darker circular features against the crystalline matrix. The density of single tracks accurately matches the nominal irradiation fluence, thus validating the experimental irradiation protocol. Detailed examination of the tracks revealed a complex core-shell structure: (i) a central amorphous core where the crystalline structure was completely disrupted, (ii) an intermediate strained crystalline shell exhibiting defected lattice. This morphology reflects the radial distribution of damage induced by the ion impact and defines the effective pinning center size. Statistical analysis of the diameter distribution, accounting for both isolated and clustered tracks treated as single effective defects, was performed and a mean column radius $r = (6 \pm 2)\,\mathrm{nm}$ was determined from unbinned data analysis and used as a reference value for the subsequent analyses.

DC resistivity measurements were employed to determine the irreversibility line (IL), from which the radius of the vortex confinement region was extracted. The obtained value, $r_0 = 5.8\,\mathrm{nm}$, showed remarkable agreement with the STEM-measured column radius, providing strong experimental validation of the Bose-glass model and demonstrating the power of correlative structural-functional analysis.

The core of the analysis was the characterization of the main superconducting parameters (such as the London penetration depth λ_L) and the vortex dynamics and pinning parameters (pinning constant k_p, vortex viscosity η, depinning and crossover frequencies ν_p, ν_c, creep factor χ, normalized pinning energy height $u = U_0/k_B T$) by a microwave CPWR method. These parameters were determined and discussed within the theoretical framework of the models by Gittleman-Rosenblum, Coffey-Clem, and Blatter et al. A first outcome of this analysis was the demonstration of how columnar defects influence the pinning parameters, leading to an overall enhancement of the pinning efficiency and, consequently, of the critical current density j_c. However, the absolute value of j_c, as well as its ratio to the depairing current density, j_c/j_0, still depends on a parameter that cannot directly be determined for the specific YBCO films investigated through the CPWR method – namely, the coherence length ξ. To determine it, a comparative analysis was carried out by combining the STEM/IL-estimated column radius with microwave measurements and theoretical treatment of j_c/j_0 as a function of the column radius following the model by Klaassen et al. [48]. All results converged into a consistent framework, enabling the determination of the coherence length and the critical current density for YBCO with irradiation-induced columnar defects, yielding – at 5 K and 1 T: $\xi = \left(1.15^{+0.11}_{-0.12}\right)\,\mathrm{nm}$, $j_c = (8.8 \pm 1.0) \cdot 10^{11}\,\mathrm{Am^{-2}}$ and $j_c/j_0 = 0.34^{+0.03}_{-0.05}$.

In conclusion, the effectiveness of combining HAADF-STEM direct imaging with CPWR microwave analysis and DC characterization has been demonstrated. This correlative methodology, integrating structural microscopy, microwave spectroscopy, DC transport measurements, and theoretical modeling, defines a robust protocol for future investigations of engineered pinning centers in superconducting films, enabling performance enhancement to be estimated directly from defect characterization. In particular, it provides guidance for heavy-ion irradiation processes: the choice of fluence, the evaluation of defect radius and track overlap, and the determination of penetration depth and pinning constant via microwave measurements together allow a quantitative prediction of the critical current density across the entire temperature range under study.

CRediT authorship contribution statement

Gianluca Ghigo: Writing – original draft, Supervision, Methodology, Investigation, Formal analysis, Conceptualization; **Mario Scuderi:** Writing – original draft, Visualization, Supervision, Methodology, Investigation, Formal analysis; **Michela Fracasso:** Writing – review & editing, Data curation; **Roberto Gerbaldo:** Investigation, Data curation; **Daniele Torsello:** Writing – review & editing, Investigation; **Laura Gozzelino:** Writing – review & editing, Supervision, Investigation.

Data availability

The data that support the findings of this study are available from the corresponding author upon reasonable request.

Declaration of competing interest

The authors declare that they have no known competing financial interests or personal relationships that could have appeared to influence the work reported in this paper.

Acknowledgment

This work received partial support from INFN-CSN5 under the SAMARA and SuperMAD experiments. TEM characterization was carried out using the facilities provided by the Italian Infrastructure Beyond-Nano UPGRADE – Materials and processes Beyond the Nanoscale.

References

[1] Li Y, Liu N, Guo Z, Chen L, Gong D, Wang D, et al. Irradiation-induced defect engineering in REBCO coated conductors: mechanisms, effects, and perspectives. Materials 2026;19:300. https://doi.org/10.3390/ma19020300

[2] Zhu Y, Cai ZX, Budhani RC, Suenaga M, Welch DO. Structures and effects of radiation damage in cuprate superconductors irradiated with several-hundred-MeV heavy ions. Phys Rev B 1993;48:6436. https://doi.org/10.1103/PhysRevB.48.6436

[3] Kwon J-H, Meng Y, Wu L, Zhu Y, Zhang Y, Selvamanickam V, et al. Extended electronic structure inhomogeneity created by double chain layer defects surrounding columnar tracks in heavy-ion irradiated $YBa_2Cu_3O_{7-\delta}$. Supercond Sci Technol 2018;31:105006. https://doi.org/10.1088/1361-6668/aad842

[4] Matsui H, Yamaguchi I. Fine structure of the tracks of several-tens-MeV au ions in $YBa_2Cu_3O_{7-x}$ studied by cross-sectional transmission electron microscopy. Nucl Instrum Methods Phys Res B 2024;547:165185. https://doi.org/10.1016/j.nimb.2023.165185

[5] Civale L, Marwick AD, Worthington TK, Kirk MA, Thompson JR, Krusin-Elbaum L, et al. Vortex confinement by columnar defects in $YBa_2Cu_3O_7$ crystals: enhanced pinning at high fields and temperatures. Phys Rev Lett 1991;67:648. https://doi.org/10.1103/PhysRevLett.67.648

[6] Hardy V, Provost J, Groult D, Simon C, Hervieu M, Raveau B. Columnar defects induced by high energy heavy ions in HTSC. Their effect on irreversibility line and pinning properties. J Alloys Compd 1993;195:395. https://doi.org/10.1016/0925-8388(93)90764-E

[7] Nakajima Y, Tsuchiya Y, Taen T, Tamegai T, Okayasu S, Sasase M. Enhancement of critical current density in co-doped $BaFe_2As_2$ with columnar defects introduced by heavy-ion irradiation. Phys Rev B 2009;80:012510. https://doi.org/10.1103/PhysRevB.80.012510

[8] Sun Y, Park A, Pyon S, Tamegai T, Kambara T, Ichinose A. Effects of heavy-ion irradiation on FeSe. Phys Rev B 2017;95:104514. https://doi.org/10.1103/PhysRevB.95.104514

[9] Massee F, Sprau PO, Wang Y-L, Davis JCS, Ghigo G, Gu GD, et al. Imaging atomic-scale effects of high-energy ion irradiation on superconductivity and vortex pinning in Fe(Se,Te). Sci Adv 2015;1:e1500033. https://doi.org/10.1126/sciadv.1500033

[10] Ghigo G, Gerbaldo R, Gozzelino L, Laviano F, Tamegai T. Effects of heavy-ion irradiation on the microwave surface impedance of $(Ba_{1-x}K_x)Fe_2As_2$ single crystals. Supercond Sci Technol 2018;31:034006. https://doi.org/10.1088/1361-6668/aaa858

[11] Lofland SE, Bhagat SM, Rajeswari M, Venkatesan T, Kanjilal D, Senapati L, et al. Microwave observation of the vortex locked-in state in $YBa_2Cu_3O_7$ thin films with columnar defects. Phys Rev B 1995;51:8489. https://doi.org/10.1103/PhysRevB.51.8489

[12] Wosik J, Xie L-M, Mazierska J, Grabovickic R. Influence of columnar defects on surface resistance of $YBa_2Cu_3O_x$ superconducting thin films; nonlinear effects. Appl Phys Lett 1999;75:1781. https://doi.org/10.1063/1.124818

[13] Ghigo G, Fracasso M, Gerbaldo R, Torsello D, Pira C, Marconato G, et al. Vortex-induced nonlinearity and the effects of ion irradiation on the high-frequency response of NbTi films. Results Phys 2024;57:107437. https://doi.org/10.1016/j.rinp.2024.107437

[14] Ghigo G, Laviano F, Gerbaldo R, Gozzelino L. Tuning the response of YBCO microwave resonators by heavy-ion patterned micro-channels. Supercond Sci Technol 2012;25:115007. https://doi.org/10.1088/0953-2048/25/11/115007

[15] Kasatkin AL, Pokusinskyi AO, Boliasova OO, Tsvitkovskyi VP, Shapovalov AP. High-frequency vortex dynamics and losses in the mixed state of nanostructured superconductors with columnar defects. Low Temp Phys 2023;49:1009. https://doi.org/10.1063/10.0020592

[16] Utz B, Semerad R, Bauer M, Prusseit W, Berberich P, Kinder H. Deposition of YBCO and NBCO films on areas of 9 in. in diameter. IEEE Trans Appl Supercond 1997;7:1272. https://doi.org/10.1109/77.620749

[17] Ghigo G, Torsello D. Microwave analysis of unconventional superconductors with coplanar-resonator techniques. Springer; 2022. https://doi.org/10.1007/978-3-030-93910-6

[18] Ziegler JF, Ziegler MD, Biersack JP. SRIM – the stopping and range of ions in matter (2010). Nucl Instrum Methods Phys Res B 2010;268:1818. https://doi.org/10.1016/j.nimb.2010.02.091

[19] Vendik OG, Vendik IB, Kaparkov DI. Empirical model of the microwave properties of high-temperature superconductors. IEEE Trans Microw Theory Tech 1998;46:469. https://doi.org/10.1109/22.668643

[20] Spence J CH. High-resolution electron microscopy. Oxford, UK: Oxford University Press; 4th ed.; 2013. ISBN 9780199668632.

[21] Phillips PJ, De Graef M, Kovarik L, Agrawal A, Windl W, Mills MJ. Atomic-resolution defect contrast in low angle annular dark-field STEM. Ultramicroscopy 2012;116:47. https://doi.org/10.1016/j.ultramic.2012.03.013

[22] Nakajima K, Morita Y, Suzuki M, Narumi K, Saitoh Y, Ishikawa N, et al. Direct observation of fine structure in ion tracks in amorphous Si_3N_4 by TEM. Nucl Instrum Methods Phys Res B 2012;291:12. https://doi.org/10.1016/j.nimb.2012.09.007

[23] Yan Y, Kirk MA. Observation and mechanism of local oxygen reordering induced by high-energy heavy-ion (U+, Au+, Xe+) irradiation in the high-T_c superconductor $YBa_2Cu_3O_{7-\delta}$. Phys Rev B 1998;57:6152. https://doi.org/10.1103/PhysRevB.57.6152

[24] Torsello D, Gerbaldo R, Gozzelino L, Laviano F, Takahashi A, Park A, et al. Twofold role of columnar defects in iron based superconductors. Supercond Sci Technol 2020;33:094012. https://doi.org/10.1088/1361-6668/aba350

[25] Silverman BW. Density estimation for statistics and data analysis. Monographs on Statistics and Applied Probability; London: Chapman and Hall; 1986. ISBN 978–0412246203.

[26] Scott DW. Multivariate density estimation: theory, practice, and visualization. Wiley Series in Probability and Statistics; Hoboken, NJ: John Wiley & Sons; 2nd ed.; 2015. ISBN 978–0471697558. https://doi.org/10.1002/9781118575574

[27] Freedman D, Diaconis P. On the histogram as a density estimator. Z F"ur Wahrscheinlichkeitstheorie Verwandte Geb 1981;57:453. https://doi.org/10.1007/BF01025868

[28] Meftah A, Brisard F, Costantini JM, Dooryhee E, Hage-Ali M, Hervieu M, et al. Track formation in SiO quartz and thermal-spike mechanism. Phys Rev B 1994;49:12457. https://doi.org/10.1103/PhysRevB.49.12457

[29] Szenes G. General features of latent track formation in magnetic insulators irradiated with swift heavy ions. Phys Rev B 1995;51:8026. https://doi.org/10.1103/PhysRevB.51.8026

[30] Ishikawa N, Nishimura Y, Oshima N, Nagashima K, Yamamura Y. Binomial distribution function for intuitive understanding of fluence dependence of non-amorphized ion-track area. Nucl Instrum Methods Phys Res B 2010;268:3273. https://doi.org/10.1016/j.nimb.2010.06.006

[31] Krusin-Elbaum L, Civale L, Blatter G, Marwick AD, Holtzberg F, Feild C. Bose-glass melting in YBaCuO crystals with correlated disorder. Phys Rev Lett 1994;72:1914. https://doi.org/10.1103/PhysRevLett.72.1914

[32] Mezzetti E, Gerbaldo R, Ghigo G, Gozzelino L, Minetti B, Camerlingo C, et al. Control of the critical current density in $YBa_2Cu_3O_{7-\delta}$ films by means of intergrain and intragrain correlated defects. Phys Rev B 1999;60:7623. https://doi.org/10.1103/PhysRevB.60.7623

[33] Ramshaw BJ, Day J, Vignolle B, LeBoeuf D, Dosanjh P, Proust C, et al. Vortex lattice melting and H_{c2} in underdoped $YBa_2Cu_3O_y$. Phys Rev B 2012;86:174501. https://doi.org/10.1103/PhysRevB.86.174501

[34] Sueyoshi T. Modification of critical current density anisotropy in high-T_c superconductors by using heavy-ion irradiations. Quantum Beam Sci 2021;5:16. https://doi.org/10.3390/qubs5020016

[35] In a previous paper [38] we already reported a fit of the irreversibility line for YBCO with columnar defects, but in that case we assumed ξ and Gi from literature. Here, we show that by making Gi explicit, there is no need to assume a value for ξ and that all the parameters (with the only exception of the anisotropy factor Γ) can be taken from the experimental microwave and DC analysis. 2026

[36] Ghigo G, Torsello D, Gozzelino L, Fracasso M, Bartoli M, Pira C, et al. Vortex dynamics in NbTi films at high frequency and high DC magnetic fields. Sci Rep 2023;13:9315. https://doi.org/10.1038/s41598-023-36473-x

[37] Gittleman JI, Rosenblum B. Radio-frequency resistance in the mixed state for subcritical currents. Phys Rev Lett 1966;16:734. https://doi.org/10.1103/PhysRevLett.16.734

[38] Ghigo G, Fracasso M, Gerbaldo R, Torsello D, Fonnesu D, Fretto M, et al. Heavy ion irradiation effects on the high-frequency properties of YBCO and Nb_3Sn thin

films. Superconductivity 2025;13:100149. https://doi.org/10.1016/j.supcon.2024.100149
[39] Blatter G, Feigel'man MV, Geshkenbein VB, Larkin AI, Vinokur VM. Vortices in high-temperature superconductors. Rev Mod Phys 1994;66:1125. https://doi.org/10.1103/RevModPhys.66.1125
[40] Golosovsky M, Tsindlekht M, Davidov D. High-frequency vortex dynamics in $YBa_2Cu_3O_7$. Supercond Sci Technol 1996;9:1. https://doi.org/10.1088/0953-2048/9/1/001
[41] Griessen R, Hai-hu W, van Dalen A JJ, Dam B, Rector J, Schnack HG, et al. Evidence for mean free path fluctuation induced pinning in $YBa_2Cu_3O_7$ and $YBa_2Cu_4O_8$ films. Phys Rev Lett 1994;72:1910. https://doi.org/10.1103/PhysRevLett.72.1910
[42] Coffey MW, Clem JR. Unified theory of effects of vortex pinning and flux creep upon the RF surface impedance of type-II superconductors. Phys Rev Lett 1991;67:386. https://doi.org/10.1103/PhysRevLett.67.386
[43] Powell JR, Porch A, Humphreys RG, Wellhöfer F, Lancaster MJ, Gough CE. Field, temperature, and frequency dependence of the surface impedance of $YBa_2Cu_3O_7$ thin films. Phys Rev B 1998;57:5474. https://doi.org/10.1103/PhysRevB.57.5474
[44] Thompson JR, Sun YR, Civale L, Malozemoff AP, McElfresh MW, Marwick AD, et al. Effect of flux creep on the temperature dependence of the current density in Y-Ba-Cu-O crystals. Phys Rev B 1993;47:14440. https://doi.org/10.1103/PhysRevB.47.14440
[45] Pompeo N, Silva E. Reliable determination of vortex parameters from measurements of the microwave complex resistivity. Phys Rev B 2008;78:094503. https://doi.org/10.1103/PhysRevB.78.094503
[46] Koshelev AE, Vinokur VM. Frequency response of pinned vortex lattice. Phys C: Supercond 1991;173:465. https://doi.org/10.1016/0921-4534(91)90749-O
[47] Tinkham M. Introduction to superconductivity. Courier Corporation; 2004.
[48] Klaassen FC, Doornbos G, Huijbregtse JM, van der Geest R CF, Dam B, Griessen R. Vortex pinning by natural linear defects in thin films of $YBa_2Cu_3O_{7-\delta}$. Phys Rev B 2001;64:184523. https://doi.org/10.1103/PhysRevB.64.184523
[49] Petrenko EV, Omelchenko LV, Terekhov AV, Kolesnichenko YA, Rogacki K, Sergeyev DM, et al. Temperature dependence of upper critical fields and coherence lengths for optimally-doped $YBa_2Cu_3O_{7-\delta}$ thin films. Low Temp Phys 2022;48:755. https://doi.org/10.1063/10.0014015
[50] Gauzzi A, Jönsson-Åkerman BJ, Clerc-Dubois A, Pavuna D. Scaling between superconducting critical temperature and structural coherence length in $YBa_2Cu_3O_{6.9}$ films. Eur Lett 2000;51:667. https://doi.org/10.1209/epl/i2000-00390-9
[51] Roas B, Hensel B, Saemann-Ischenko G, Schultz L. Irradiation-induced enhancement of the critical current density of epitaxial $YBa_2Cu_3O_{7-x}$ thin films. Appl Phys Lett 1989;54:1051. https://doi.org/10.1063/1.101423
[52] Ohshima S, Oikawa S, Noguchi T, Inadomaru M, Kusunoki M, Mukaida M, et al. The correlation of the critical current density and surface resistance of $YBa_2Cu_3O_{7-\delta}$ thin films. Phys C: Supercond 2002;372–376:671. https://doi.org/10.1016/S0921-4534(02)00827-4
[53] Stangl A, Palau A, Deutscher G, Obradors X, Puig T. Ultra-high critical current densities of superconducting $YBa_2Cu_3O_{7-\delta}$ thin films in the overdoped state. Sci Rep 2021;11:8176. https://doi.org/10.1038/s41598-021-87639-4
[54] van der Beek CJ, Konczykowski M, Abal'oshev A, Abal'osheva I, Gierlowski P, Lewandowski SJ, et al. Strong pinning in high-temperature superconducting films. Phys Rev B 2002;66:024523. https://doi.org/10.1103/PhysRevB.66.024523
[55] Dotsenko VP, Mancini A, Armenio AA, Rufoloni A, Fava A, Sotgiu G, et al. Optimization of high-quality YBCO thin films deposited by PLD as a function of thickness. IEEE Trans Appl Supercond 2026;36:1. https://doi.org/10.1109/TASC.2026.3652031
[56] Paturi P, Aye MM, Soman A, Notthoff C, Kluth P, Strickland N, et al. Verifying theoretical models of flux pinning using heavy ion irradiated YBCO thin films. IEEE Trans Appl Supercond 2025;35:1. https://doi.org/10.1109/TASC.2025.3527949
[57] Zhang H, Ding F, Gu H, Dong Z, Qu F. Fabrication of high-j_c $BaTiO_3$-doped $YBa_2Cu_3O_{7-\delta}$ thin films by the low-fluorine TFA-MOD approach. J Alloys Compd 2016;664:5. https://doi.org/10.1016/j.jallcom.2015.12.220
[58] Kosse AI, Prokhorov AY, Khokhlov VA, Levchenko GG, Semenov AV, Kovalchuk DG, et al. Measurements of the magnetic field and temperature dependences of the critical current in YBCO films and procedures for an appropriate theoretical model selection. Supercond Sci Technol 2008;21:075015. https://doi.org/10.1088/0953-2048/21/7/075015
[59] Golovchanskiy IA, Pan AV, Shcherbakova OV, Fedoseev SA, Dou SX. An all-field-range description of the critical current density in superconducting YBCO films. Supercond Sci Technol 2011;24:105020. https://doi.org/10.1088/0953-2048/24/10/105020